

Imidazolinium-based Multiblock Amphiphile as Transmembrane Anion Transporter

Miki Mori,^[a] Kohei Sato,^{*[a]} Toru Ekimoto,^{*[b]} Shinichi Okumura,^[b] Mitsunori Ikeguchi,^{*[b, c]} Kazuhito V. Tabata,^{*[d]} Hiroyuki Noji,^{*[d]} and Kazushi Kinbara^{*[a]}

Abstract: Transmembrane anion transport is an important biological process in maintaining cellular functions. Thus, synthetic anion transporters are widely developed for their biological applications. Imidazolinium was introduced as anion recognition site to a multiblock amphiphilic structure that consists of octa(ethylene glycol) and aromatic units. Ion transport assay using halide-sensitive lucigenin and pH-sensitive 8-hydroxypyrene-1,3,6-trisulfonate (HPTS) revealed that imidazolinium-based multiblock amphiphile (IMA) transports anions and showed high selectivity for nitrate, which

plays crucial roles in many biological events. Temperature-dependent ion transport assay using 1,2-dipalmitoyl-*sn*-glycero-3-phosphocholine (DPPC) indicated that IMA works as a mobile carrier. ¹H NMR titration experiments indicated that the C2 proton of the imidazolinium ring recognizes anions via a (C–H)⁺...X[–] hydrogen bond. Furthermore, all-atom molecular dynamics simulations revealed a dynamic feature of IMA within the membranes during ion transportation.

Introduction

Ion homeostasis of the cells is essential element in maintaining life. Generation and preservation of ion concentration gradient means regulation of pH, cellular volumes or membrane potentials, which plays crucial roles in diverse cellular functions such as apoptosis, differentiation and proliferation.^[1] Regulation of ion concentration is achieved by membrane transporters embedded within the lipid bilayer membranes, by controlling transported ionic species and their directions. However, genetic diseases may trigger disordered ion transport. Synthetic membrane transporters, especially anion transporters, are eagerly developed for their potentials in biological applications and therapeutics for diseases related to dysfunction of membrane transporters, including cystic fibrosis.^[2] Among the anions,

nitrate, abundant in our everyday diet, had been believed as a harmful species to promote gastric cancer, as well as an inert product of nitrogen oxide (NO) metabolism. Meanwhile, recent studies indicated that nitrate is a substrate for generating bioactive NO through the nitrate-nitrite-NO metabolism pathway, where such a metabolization pathway also mediates cell signaling and blood flow regulation. It is also considered to play a therapeutic role in cardiovascular diseases.^[3]

Natural membrane proteins have very complex structures depending on their target ions and transport mechanisms,^[4] and only a few natural anion carriers are known to exist.^[5] Despite lack in structural motifs in natural systems, various structures have emerged as synthetic anion transporters, recognizing anions through anion- π interaction, electrostatic interactions, halogen bonds, chalcogen bonds and hydrogen bonds.^[5,6] Although C–H...X[–] hydrogen bond had emerged as another important noncovalent anion recognition strategy in developing anion receptors,^[7] its role had been supplementary in transport systems of mobile carriers.^[8] Anion transporters that strongly rely on C–H...X[–] hydrogen bonds are still rare compared to those bearing traditional N–H and O–H hydrogen bond donors.^[9,10]

Previously, our group has reported series of multiblock amphiphiles capable of ion transport as channels. They consist of alternated structure of hydrophilic oligo(ethylene glycol) chains and hydrophobic aromatic moieties, which self-assemble by π -stack of aromatic moieties within the lipid bilayer membranes. The designs of these molecules were derived from multipass transmembrane proteins, which exhibit their functions by folding within the lipid bilayers.^[11–14] Variable designs in hydrophobic moieties had enabled to develop diverse characteristics in ion transportation. Membrane-tension responsive ion channel formation was achieved by destabilization of aromatic stacking by introducing sterically hindered aromatic unit.^[12] Reversible ligand-gating ion transport was realized by incorpo-

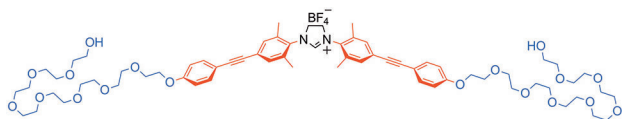
[a] M. Mori, Dr. K. Sato, Prof. K. Kinbara
School of Life Science and Technology
Tokyo Institute of Technology
4259 Nagatsuta-cho, Midori-ku, Yokohama, Kanagawa, 226-8501 (Japan)
E-mail: koheisato@bio.titech.ac.jp
kkinbara@bio.titech.ac.jp

[b] Dr. T. Ekimoto, S. Okumura, Prof. M. Ikeguchi
Graduate School of Medical Life Science
Yokohama City University
1-7-29 Suehiro-cho, Tsurumi-ku, Yokohama, Kanagawa, 230-0045 (Japan)
E-mail: ekimoto@yokohama-cu.ac.jp
ike@yokohama-cu.ac.jp

[c] Prof. M. Ikeguchi
RIKEN Medical Science Innovation Hub Program
1-7-22 Suehiro-cho, Tsurumi-ku, Yokohama, Kanagawa, 230-0045 (Japan)
E-mail: ike@yokohama-cu.ac.jp

[d] Prof. K. V. Tabata, Prof. H. Noji
Graduate School of Engineering
University of Tokyo
7-3-1 Hongo, Bunkyo-ku, Tokyo, 113-8656 (Japan)
E-mail: kazuhito@nojiab.t.u-tokyo.ac.jp
hnoji@appchem.t.u-tokyo.ac.jp

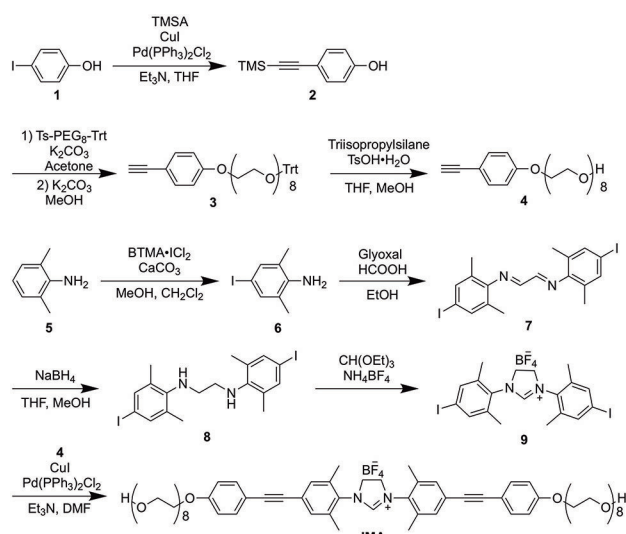
Supporting information for this article is available on the WWW under <https://doi.org/10.1002/asia.202001106>



Scheme 1. Molecular structure of **IMA**. Hydrophobic, hydrophilic, and imidazolium moieties are indicated in red, blue, and black, respectively.

ration of ligand-binding phosphoric ester group to the boundary of hydrophilic and hydrophobic units.^[13,14] Therefore, designing suitable hydrophobic unit is necessarily in developing diverse synthetic ion transport systems by multiblock amphiphile.

Herein, we applied this concept of molecular design to develop a new synthetic anion transporter. Non-ionic, hydrophilic octa(ethylene glycol) (OEG) chains are located on the one end of hydrophobic diphenylacetylene units following our previously developed multiblock amphiphilic compounds.^[11–14] In addition, imidazolium was introduced to the center of the hydrophobic moiety, in between two diphenylacetylene units, as an anion recognition site (Scheme 1). The C2 proton of the imidazolium ring is able to act as a (C–H)⁺...X[–] hydrogen bond donor,^[7] which we expected to be the major interaction for anion recognition. Interestingly, this imidazolium-based multiblock amphiphile (**IMA**) transported ions as a mobile carrier rather than forming transmembrane channel, with selectivity for nitrate.



Scheme 2. Synthetic scheme of **IMA**. (TMSA = trimethylsilylacetylene, Ts = (4-methylphenyl)sulfonyl, Trt = triphenylmethyl, BTMA = benzyltrimethylammonium).

Results and Discussion

Synthesis

IMA was synthesized following Scheme 2, where hydrophilic octa(ethylene glycol) derivative (**4**) and iodinated imidazolium salt (**9**) were synthesized individually. Initially, **2** was synthesized by Sonogashira coupling^[15] of **1** and trimethylsilylacetylene (TMSA). Ts-OEG-Trt was synthesized following the procedures reported in our previous paper.^[16] **2** and Ts-OEG-Trt were coupled by Williamson ether synthesis, followed by deprotection of Trt group to afford **4**. Meanwhile, **9** was synthesized using reductive amination of glyoxal with **6**, followed by cyclization using triethyl orthoformate. Finally, compound **4** and **9** were conjugated via Sonogashira coupling to afford **IMA**. See Experimental Section for details on these procedures and characterizations.

Ion transport activity of **IMA**

Large unilamellar vesicles (LUVs) of 1,2-dioleoyl-*sn*-glycero-3-phosphocholine (DOPC) encapsulating pH sensitive 8-hydroxyppyrene-1,3,6-trisulfonate (HPTS) were prepared for evaluation of the ion transport activity of **IMA**. An aqueous solution of **IMA** was added externally to the DOPC LUV suspension in a 4-(2-hydroxyethyl)-1-piperazineethanesulfonic acid (HEPES) buffer including NaCl (50 mM), with pH gradient (intravesicular pH 7.1 and extravesicular pH 7.9) across the membranes. **IMA** mediated ion transportation would result in increase of intravesicular pH, leading to deprotonation of HPTS which enhances its fluorescence.

First, ion transport activity of **IMA** was investigated at **IMA** concentration of 2 μ M. As a result, significant increase in the fluorescence intensity was observed just after addition of **IMA** (Figure 1a, blue plots), indicating that **IMA** is capable of

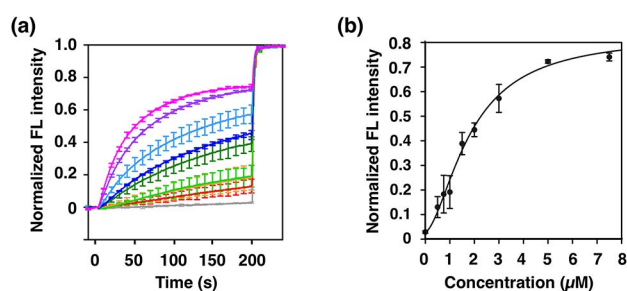


Figure 1. (a) Time course change of HPTS fluorescence intensity ($\lambda_{em} = 510$ nm, $\lambda_{ex} = 460$ nm) encapsulated in DOPC LUVs upon addition of **IMA** at 0 s, with various **IMA** concentrations; 0 μ M (grey), 0.5 μ M (red), 0.75 μ M (orange), 1.0 μ M (light green), 1.5 μ M (green), 2.0 μ M (blue), 3.0 μ M (light blue), 5.0 μ M (purple) and 7.5 μ M (pink). All measurements were carried out with 200 μ M DOPC at 20 °C; 20 mM HEPES, 50 mM NaCl, 30 μ M HPTS, pH 7.1 as an internal buffer; 20 mM HEPES, 50 mM NaCl, pH 7.9 as an external buffer. Data are averages of three independent measurements, with error bars indicating standard deviation at every 10 s (extracted for clarity). (b) Normalized fluorescence intensity of HPTS encapsulated in DOPC LUVs at 200 s after addition of **IMA** as a function of **IMA** concentration. The solid line represents a curve-fit analysis with the Hill equation.^[17]

transmembrane ion transport. In addition, we carried out conductance measurement with a planar lipid bilayer (Figure S1, Supporting Information), which also displayed the ion transportation capability of *IMA*. This was further confirmed by changing the concentration of *IMA* from 0 μM to 7.5 μM , to result in concentration dependent ion transport activity (Figure 1a). The ion transportation efficiency of *IMA* was investigated by plotting HPTS fluorescence intensity encapsulated in DOPC LUVs at 200 s against *IMA* concentration, where the Hill coefficient (n)^[17] and effective concentration (EC_{50}) were evaluated as $n = 1.69 (\pm 0.10)$ and $\text{EC}_{50} = 1.84 (\pm 0.07) \mu\text{M}$ ($R^2 = 0.991$) (Figure 1b), respectively.^[18]

Next, we explored the species of ions *IMA* transports. Therefore, ion transportation assay was carried out by individually changing the cations and anions of extravesicular buffer salts, while the intravesicular buffer was fixed to NaCl throughout the measurements.^[19] Indeed, cation selectivity was determined by using Li^+ , Na^+ , K^+ , Rb^+ , and Cs^+ as extravesicular cations. In this case, *IMA* did not show significant dependence in the change of HPTS fluorescence intensity on cations (Figure 2a). This suggests that *IMA* does not facilitate transport of cations, unlike our previously reported multiblock amphiphile, which showed ion transport efficiency depending on the cationic species.^[11] Then, we assumed that anionic species are

responsible for ion transport efficiency by *IMA*, and anion selectivity was examined by using Cl^- , Br^- , I^- , NO_3^- , and ClO_4^- as extravesicular anions. In sharp contrast to the result on the cation selectivity investigation, *IMA* showed significant difference in the change of HPTS fluorescence intensity, in the order of $\text{NO}_3^- > \text{ClO}_4^- > \text{Cl}^- > \text{Br}^- > \text{I}^-$ (Figure 2b), at 200 s after addition of *IMA*. Results from these two experiments strongly suggest that *IMA* mediates transport of anions.

Since HPTS based assays allow for only indirect observation of anion transport, we carried out ion transport assay using a halide sensitive dye, lucigenin.^[19,20] Lucigenin fluorescence quenches in the presence of Cl^- . We prepared DOPC LUVs encapsulating lucigenin in a HEPES buffer including NaNO_3 (50 mM) without pH gradient across the membranes. Cl^- was introduced only to the extravesicular buffer solution to create Cl^- concentration gradient (Figure 2c). If *IMA* should transport Cl^- , influx of Cl^- can be detected as quenching of lucigenin fluorescence encapsulated in DOPC LUVs. In fact, upon addition of *IMA* at 2 μM , lucigenin fluorescence quenched drastically (Figure 2d, green line), indicating the influx of Cl^- . This was further confirmed by varying *IMA* concentration from 0 μM to 7.5 μM , which resulted in concentration dependent Cl^- influx (Figure 2d). These results strongly indicate that Cl^- is the transported species, thereby suggesting that *IMA* transports anions. The anion selectivity trend we observed ($\text{NO}_3^- > \text{ClO}_4^- > \text{Cl}^- > \text{Br}^- > \text{I}^-$) (Figure 2b) mostly follows hard and soft, acid and base (HSAB) principle,^[21] relatively hard bases are likely being transported efficiently by a hard cationic proton donor like *IMA*.

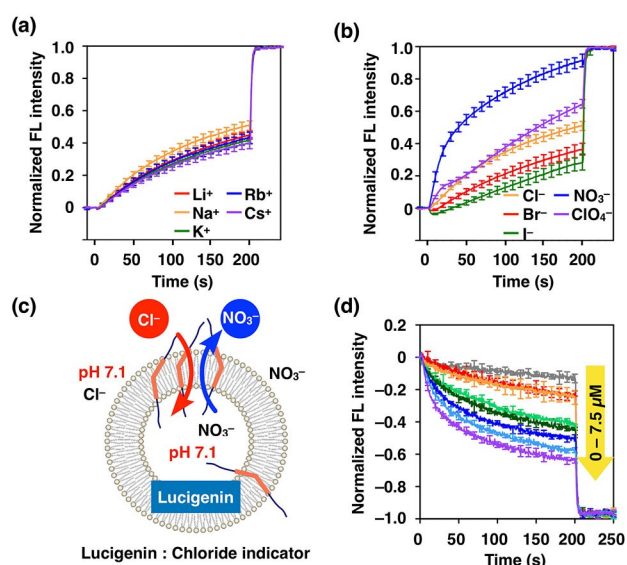


Figure 2. (a) and (b) Time course change of HPTS fluorescence intensity ($\lambda_{\text{em}} = 510 \text{ nm}$, $\lambda_{\text{ex}} = 460 \text{ nm}$) encapsulated in DOPC LUVs in a HEPES buffer upon addition of *IMA* with different cations (Li^+ , Na^+ , K^+ , Rb^+ , Cs^+ , $\text{X}^- = \text{Cl}^-$ (a)) and different anions (Cl^- , Br^- , I^- , NO_3^- , ClO_4^- , $\text{M}^+ = \text{Na}^+$ (b)). Measurements were carried out at $[\text{DOPC}] = 200 \mu\text{M}$, $[\text{IMA}] = 2 \mu\text{M}$ at 20°C , where an intravesicular buffer is 20 mM HEPES, 50 mM NaCl, 30 μM HPTS, pH 7.1 and an extravesicular buffer is 20 mM HEPES, 50 mM MX, pH 7.9. (c) Schematic illustration of lucigenin assay. (d) Time course change of lucigenin fluorescence intensity ($\lambda_{\text{em}} = 535 \text{ nm}$, $\lambda_{\text{ex}} = 450 \text{ nm}$) encapsulated in DOPC LUVs at various *IMA* concentrations; 0 μM (grey), 0.75 μM (red), 1.0 μM (orange), 1.5 μM (light green), 2.0 μM (green), 3.0 μM (blue), 5.0 μM (light blue) and 7.5 μM (purple). An intravesicular buffer (pH 7.1) contains 300 μM lucigenin, 20 mM HEPES, 50 mM NaNO_3 , and an extravesicular buffer (pH 7.1) contains 20 mM HEPES, 50 mM NaNO_3 , and NaCl aq. was added to reach final concentration of 10 mM. Data are averages of three measurements, with error bars indicating standard deviation at every 10 s (extracted for clarity).

Mechanism of ion transport by *IMA*

Then, we identified the anionic species transported by *IMA*. The electric charge balance of the intravesicular and extravesicular buffers was kept neutral through the ion transport process. First, transport rate of H^+ and X^- was compared by performing HPTS assay in the presence and absence of carbonyl cyanide 4-(trifluoromethoxy)phenylhydrazone (FCCP), a highly active H^+ carrier. When FCCP was incorporated in the membrane with pH gradient (intravesicular pH 7.1 and extravesicular pH 7.9), FCCP transports H^+ to decrease the H^+ gradient, meaning efflux in this system (Figure 3a). H^+ efflux leads to decrease in the positive charge of the inner aqueous layer. To maintain the neutral charge balance, *IMA* would transport either H^+ or X^- . Actually, transport activity of *IMA* showed a large enhancement (72%–41%–(4%–1%) = 28%) in the presence of FCCP (Figure 3b, red line). Such cooperativity in transport indicates that transport rate of X^- by *IMA* is higher than that of H^+ .^[22–24]

Then, the transported X^- was further determined by employing valinomycin, a K^+ selective carrier. In this assay, K^+ was included in the extravesicular buffer, instead of Na^+ used in the FCCP assay (Figure 3c). Here, we confirmed that 12.5 pM valinomycin itself induced a slight increase in the intravesicular HPTS fluorescence (6%–1% = 5%, Figure 3d, green line), meaning that anion transporter is also necessary for transport of K^+ by valinomycin. In other words, valinomycin induced K^+ influx leads to increase of the positive charge at the inner aqueous

layer, which also requires transport of anions so as to maintain the electric charge balance neutral. Under the conditions of this valinomycin assay, **IMA** is considered to transport either OH^- or Cl^- . Therefore, only the case of faster transport of OH^- than Cl^- should result in the larger enhancement of HPTS fluorescence than that in the case **IMA** transports the anion alone. Actually, the enhancement of HPTS fluorescence triggered by **IMA** addition in the presence and the absence of valinomycin were almost identical (Figure 3d, red and blue lines, 39% in both conditions), implying no cooperativity of ion transportation by valinomycin and **IMA**. Such lack in the cooperativity strongly indicates that Cl^- transport is dominant while OH^- transport is negligible.

Another possibility we need to consider in valinomycin assay is H^+/M^+ antiport, where H^+ efflux in exchange to K^+ influx by valinomycin. However, taking the lack in the cation selectivity of **IMA** into account (Figure 2a), **IMA** is not likely to transport cations, suggesting that H^+/M^+ antiport is also negligible.^[23]

Influence of membrane fluidity on ion transport by **IMA**

We then had interest in how **IMA** transports anions through the lipid bilayer membranes at the molecular level. There are two possible mechanisms of transmembrane ion transport by molecular species, i.e. transporting ions through the formation of an ion channel or as a mobile carrier. Ion channels form pores for ions to pass through the membranes, whereas mobile carriers bind with anions and diffuse across the membranes. Therefore, ion transport efficiency of mobile carriers strongly depends on the membrane fluidity since diffusion is restricted in the membranes with low fluidity, while ion channels are not significantly affected, as transmembrane diffusion is less important.^[25–27] Thus influence of the membrane fluidity was investigated using 1,2-dipalmitoyl-*sn*-glycero-3-phosphocholine (DPPC) instead of DOPC for HPTS assay. DPPC adopts highly fluid liquid phase above the phase transition temperature ($T_m = 41^\circ\text{C}$), and much less fluid gel phase below T_m . We prepared DPPC LUVs encapsulating HPTS at pH 7.1, and added a **IMA** solution at 50°C (liquid phase) to enhance the incorporation of **IMA** to the membranes. Then, temperature was changed to either 50°C or 20°C (gel phase), followed by addition of NaOH aq. for generation of pH gradient across the membranes to initiate the ion transport by **IMA** incorporated within the membranes (Figure 3e). As a result, significant increase of HPTS fluorescence was observed at 50°C (Figure 3f, red line) compared to the blank measurement at 50°C (Figure 3f, grey line), whereas increase of HPTS fluorescence at 20°C (Figure 3f, blue line) was almost identical to the blank measurement at 20°C (Figure 3f, black line). These results indicate that **IMA** is capable of ion transport only through the liquid phase membranes, thereby indicating **IMA** acts as a mobile carrier. Mobile carrier mechanism is a unique property of **IMA**, since our previously reported multiblock amphiphiles were all channel-forming molecules.^[11–14]

^1H NMR titration

The anion binding property of **IMA** was evaluated by ^1H NMR titration in CDCl_3 , using tetrabutylammonium chloride (TBACl) as Cl^- source. **IMA** concentration was fixed to 1 mM throughout the measurements whereas TBACl concentration was varied. Upon increasing the TBACl concentration, chemical shift of H_a exhibited down field shift of $\Delta\delta = 1.48$ ppm, which is indicative of the interaction between Cl^- and H_a via $(\text{C}-\text{H})^+\cdots\text{X}^-$ hydrogen bond (Figure 4b). In addition, ^1H chemical shifts of the protons around the aromatic ring also changed, exhibiting up field shifts

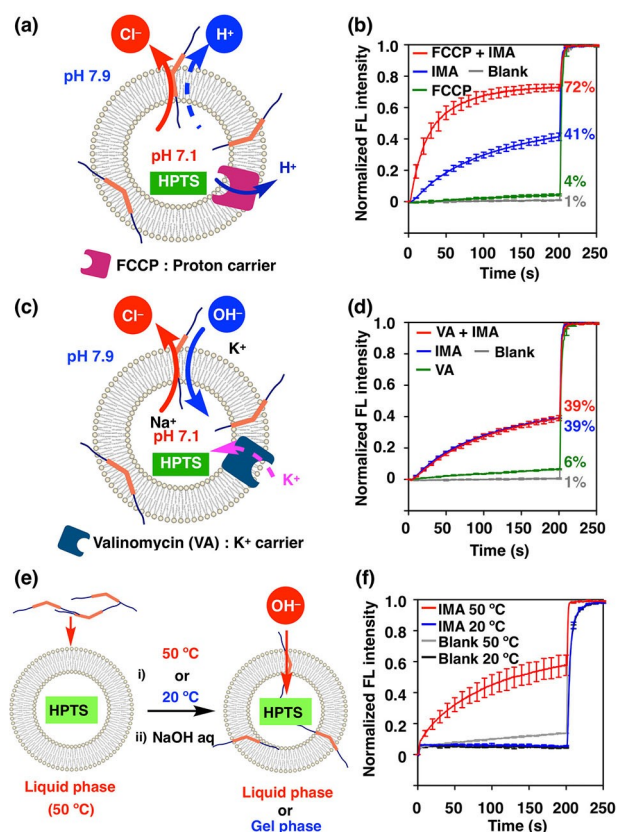


Figure 3. (a) Schematic illustration of HPTS assay in the presence of FCCP. (b) Comparison of ion transport in the presence and absence of FCCP (1 μM) with or without **IMA** (2 μM). Measurements were carried out at $[\text{DOPC}] = 200 \mu\text{M}$, 20°C , with an intravesicular buffer (pH 7.1) containing 20 mM HEPES, 50 mM NaCl, 30 μM HPTS, and an extravesicular buffer (pH 7.9) containing 20 mM HEPES, 50 mM NaCl. (c) Schematic illustration of HPTS assay in the presence of valinomycin. (d) Comparison of ion transport in the presence and absence of valinomycin (VA, 12.5 μM) with or without **IMA** (2 μM). Measurements were carried out at $[\text{DOPC}] = 200 \mu\text{M}$, 20°C , with an intravesicular buffer (pH 7.1) containing 20 mM HEPES, 50 mM NaCl, 30 μM HPTS, and an extravesicular buffer (pH 7.9) containing 20 mM HEPES, 50 mM NaCl. (e) Schematic illustrations of the assay using DPPC to investigate the influence of membrane fluidity on ion transport by **IMA**. **IMA** was introduced into the membranes at 50°C (liquid phase), followed by i) equilibration of measurement temperature to 50°C (liquid phase) or 20°C (gel phase) and ii) pH gradient generation upon addition of NaOH aq. to the extravesicular buffer for initiation of ion transport. (f) Time course change of HPTS fluorescence encapsulated in DPPC LUVs with or without **IMA** at 50°C or 20°C . Measurements were carried out at $[\text{IMA}] = 0.25 \mu\text{M}$, $[\text{DPPC}] = 200 \mu\text{M}$, 20 mM HEPES, 50 mM NaCl, 30 μM HPTS as an intravesicular buffer, and 20 mM HEPES, 50 mM NaCl as an extravesicular buffer. Data are averages of three measurements, with error bars indicating standard deviation at every 10 s (extracted for clarity).

for H_d and H_e (Figure 4c), and down field shift for H_c (Figure 4e). These indicate the presence of the interaction between Cl^- and aromatic rings (e.g. anion- π interaction or hydrogen bond) in addition to $(C-H)^+ \cdots X^-$ hydrogen bond of H_a . Curve fitting-analysis of the chemical shifts of H_b by BindFit v0.5^[28,29] suggest the stoichiometry of *IMA* and Cl^- to be 2:1, where the association constants were evaluated as $K_{11} = 1.69 \times 10^2 M^{-1}$ (error: $\pm 9.35\%$) and $K_{21} = 2.02 \times 10^2 M^{-1}$ (error: $\pm 4.83\%$).^[30,31]

Fluorescence depth quenching

In our previous work, we reported that the hydrophobic units of channel-forming multiblock amphiphiles prefer to be located at the hydrophobic environment of the lipid bilayers, rather than its interface.^[11] Since *IMA* behaved as a mobile carrier differently from the precedent multiblock amphiphiles which formed ion channels, we also investigated the location of *IMA* within the lipid bilayers by fluorescence depth quenching experiment.^[32] We prepared DOPC LUVs at pH 7.1 in the presence of any of the following spin-labeled lipids individually: 1-palmitoyl-2-stearoyl-(5-doxyl)-*sn*-glycero-3-phosphocholine (5-doxyl PC), 1-palmitoyl-2-stearoyl-(12-doxyl)-*sn*-glycero-3-phosphocholine (12-doxyl PC), or 1-palmitoyl-2-stearoyl-(16-doxyl)-*sn*-glycero-3-phosphocholine (16-doxyl PC), which bear spin probes at the different positions of the alkyl chains. *IMA* gives a fluorescence emission due to the diphenylacetylene units, which is possibly quenched by spin probes. The efficiency of fluorescence quenching within the membrane would be informative of the location of the *IMA* molecule inside the

membranes, since the quenching efficiency depends on the distance of the diphenylacetylene units from the spin labels. Indeed, membranes with 5-doxyl PC showed the highest quenching of 34% (Figure 5, red line), while those of 12-doxyl PC and 16-doxyl PC were 22% and 19%, respectively (Figure 5, blue and green lines). These comparisons suggest that *IMA* tends to locate close to the surface of the membrane rather than its hydrophobic center. We assume that the imidazolium moiety prefers aqueous environment to the hydrophobic environment of lipid bilayer membrane to allow recognition of anions. Anion binding leads to neutralization of the plus charge of the imidazolium moiety, which enables *IMA* to cross the hydrophobic layer of the membranes.

Molecular Modeling

To obtain explicit molecular models of *IMA* in the membrane-water system, all-atom molecular dynamics (MD) simulations were performed. As the initial structures for the MD simulations, *IMA* was embedded in the DOPC lipid bilayer membrane: The imidazolium ring was placed in the center of the membrane, and the orientation of the hydrophobic moiety was set to the perpendicular or parallel to the membrane (Figure S3). To mimic a situation during the anion transport, one Cl^- ion was placed near the C2 proton of the imidazolium ring. Three independent 1- μs simulations were carried out from 4 initial models (12 μs in total). During a 1 μs simulation, the hydrophobic moiety moved to the surface of the membrane near the phosphorus atoms (black, red, and blue in Figure 6a), and the L-shape conformation was observed at the surface: One OEG chain (magenta in Figure 6a) was buried in the membrane and the other OEG chain (cyan in Figure 6a) exposed to the water-membrane interface (Figure 6b). In all the simulations, the hydrophobic moiety of *IMA* was located at the surface of the

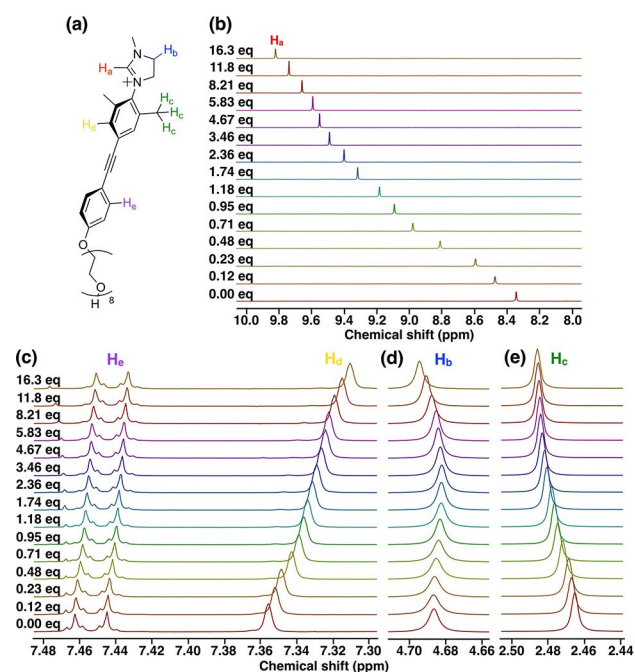


Figure 4. (a) Identification of protons. 1H NMR spectra of $[IMA] = 1$ mM with various equivalents of TBACl in $CDCl_3$ corresponding to (b) H_a , (c) H_b and H_d , (d) H_b , and (e) H_c . The equivalents of TBACl are denoted at the left side of spectra. All measurements were carried out at 25 °C.

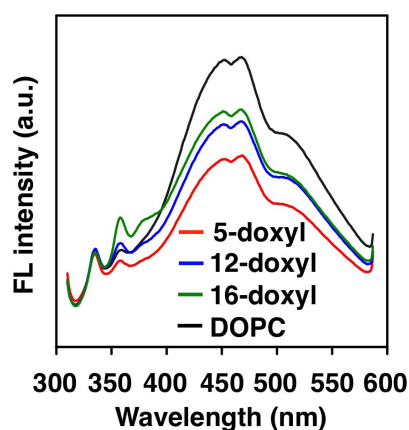


Figure 5. Fluorescence spectra of *IMA* in LUVs at ratio of $[IMA]/[total PC] = 5/200$ with excitation at 300 nm. All measurements were carried out at $[total PC] = 200 \mu M$ in 20 mM HEPES, 50 mM NaCl, pH 7.1 at 20 °C. As membrane constituents, DOPC (black line) and DOPC containing 10 mol% of 5-doxyl PC (red line), 12-doxyl PC (blue line), or 16-doxyl PC (green line) were used.

membrane rather than the center of membrane (Figures S4–6), which was in good agreement with the experimental results of the fluorescence depth quenching. Interestingly, the L-shape conformation was observed in the last stage of the most MD simulations, even though the simulations were started from various initial models (Figures S4, S5).

The interaction between the Cl^- ion and the imidazolium ring was stable during the movement of *IMA* from the center to the surface of the membrane (Figures 6a, S7). During the movement of *IMA*, the Cl^- ion was located near the C2 proton (Figures 6c, S7), and the Cl^- ion held its position without exceeding the methyl group of the diphenylacetylene unit. These interaction manners are consistent with those revealed by ^1H NMR experiments. At the membrane surface, water molecules came to be close to the Cl^- ion, and, due to the weakening of the interaction, the Cl^- ion dissociated from *IMA* (Figure S8).

Since the experimental Hill coefficient ($n=1.69$) suggested that the number of transport molecules involved in the anion transport process is possibly two, the 2:1 binding-stoichiometry model for *IMA* and the Cl^- ion was further examined. As the initial model of the dimer *IMA* simulation, the imidazolium ring of one *IMA* was placed in the center of the membrane (green in Figure S11), one Cl^- ion was placed near the C2

proton, and the other *IMA* (magenta in Figure S11) was placed so as to sandwich the Cl^- ion between the two *IMAs*. The orientation of the hydrophobic moieties of the *IMA* dimer was set to the perpendicular or parallel to the membrane. Three independent 1- μs simulations were carried out from the two initial models (6 μs in total). Except for one simulation (described later), the hydrophobic moieties of the *IMA* dimer moved to the membrane surface as was so for the 1:1 stoichiometry model described above (Figures S12–15). In the simulations starting from the perpendicular model, both the two *IMAs* formed the L-shape conformation at the surface. By contrast, in the simulations starting from the parallel model, one *IMA* formed the L-shape conformation, and the other *IMA* formed the V-shape conformation in which both OEG chains exposed to the water-membrane surface. In addition, regardless of the initial models, the two *IMAs* formed a dimer during the transport of the Cl^- ion from the center of the membrane to the membrane-water surface. However, after the Cl^- ion dissociated from the dimer, the two *IMAs* did not form a stable dimer and were sometimes separated from each other (Figure S13).

In one simulation starting from the parallel model, the *IMA* dimer was stably present in the membrane with the Cl^- ion sandwiched between the two *IMAs* during 1 μs (Figure 7a). At the first stage, the two *IMAs* formed a dimer structure with the V-shape conformations facing each other (Figure 7b), and, in

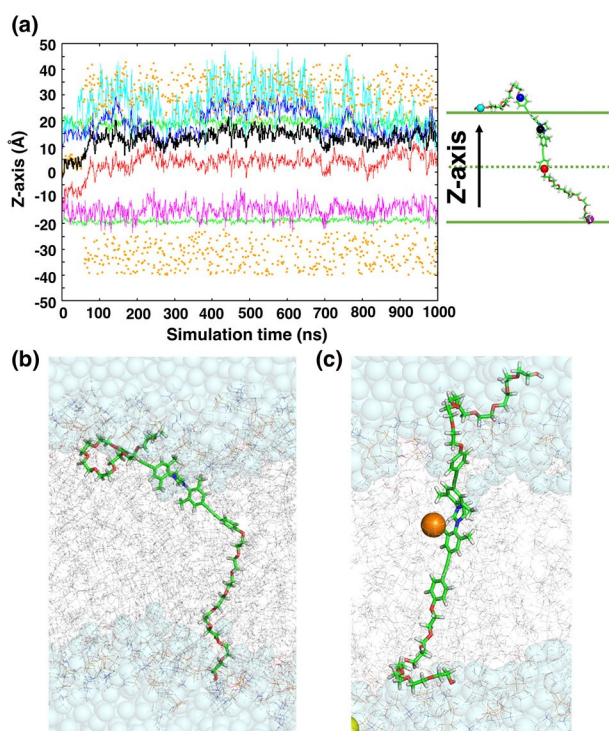


Figure 6. Structure models of *IMA* in the membrane-water system from all-atom molecular dynamics simulations. (a) The time evolution of the z-coordinate of the *IMA* and a Cl^- ion (orange). The trajectories of five carbon atoms at the imidazolium (black), the edges of the diphenylacetylene units (red and blue) and OEG chains (magenta and cyan) are plotted, and the carbon atoms are shown as spheres in the schematic figure. The average coordinates of the phosphorus atoms of the upper and lower membrane molecules are shown in green. Snapshots at (b) 1 μs and (c) 54.4 ns are illustrated.

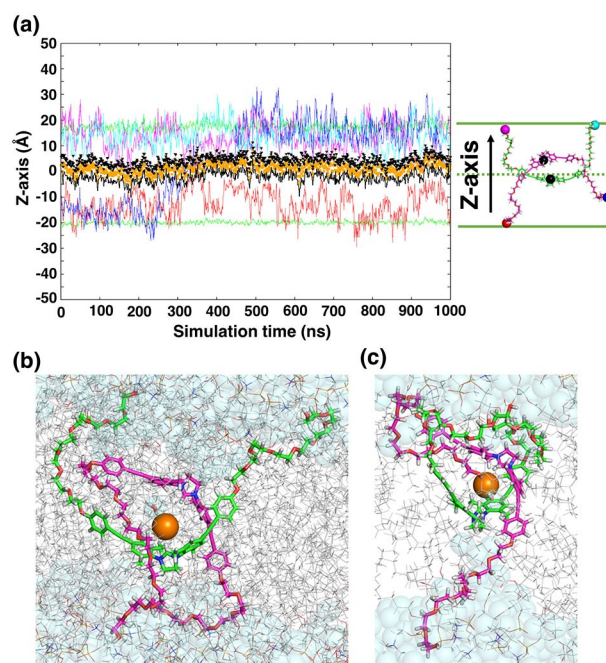


Figure 7. Structure models of *IMA* dimer in the membrane-water system from all-atom molecular dynamics simulations. (a) The time evolution of the z-coordinate of the two *IMAs* and a Cl^- ion (orange). The trajectories of three carbon atoms for each *IMA* (green, magenta in the schematic figure) at the imidazolium (black solid line, black triangle plot) and the edges of the OEG chains (magenta and cyan, red and blue) are plotted, and the carbon atoms are shown as spheres in the schematic figure. The average coordinates of the phosphorus atoms of the upper and lower membrane molecules are shown in green. Snapshots at (b) 300 ns and (c) 1 μs are illustrated.

the latter half, they formed an LV-shape conformation in which one was L-shape conformation and the other was V-shape conformation (Figure 7c). The relative position between the two imidazolium rings was maintained in the perpendicular direction of the membrane, and the fact that one IMA forming the L-shape conformation acted as a lid seemed to be the reason why the Cl⁻ ion could be retained structurally (Figure S16).

Compared with the 1:1 binding-stoichiometry model, the 2:1 model had more structural variations that could stably transport the Cl⁻ ion in the membrane. In both the stoichiometry models, the interaction manner between one IMA and the Cl⁻ ion was essentially identical. However, even with the L-shape conformation, the IMA dimer could sandwich the Cl⁻ ion at the membrane surface (Figure S17), and, therefore, the interaction between IMA and the Cl⁻ ion was retained for a long time. The V-shape conformation of one IMA held the Cl⁻ ion stably for a short time, and however, the LV-shape conformation of the IMA dimer allowed the Cl⁻ ion to be held for a long time (Figure 7). In addition, according to the interaction energy between IMA and the Cl⁻ ion during the anion transport, the IMA dimer showed more stable interaction energy than the IMA monomer (Figure S18). Taken together, for the anion transport in the membrane, the 2:1 binding-stoichiometry model was preferable, which was in good agreement with the experimental Hill analysis.

Conclusion

In conclusion, transmembrane anion transport properties of imidazolium-based multiblock amphiphile (IMA) were reported. The imidazolium ring, which was introduced at the center of the hydrophobic unit, played crucial role in anion transport. It recognizes anions via a (C-H)⁺...X⁻ hydrogen bond, as demonstrated in NMR experiments. Interestingly, the ion transport activity of IMA depended on the membrane fluidity, which is a unique property of IMA working as a mobile carrier, though alternated structure of hydrophilic and hydrophobic units is structural motif of transmembrane proteins. Furthermore, fluorescence depth quenching experiments revealed that the hydrophobic unit of IMA is located at the surface of the lipid bilayer membranes. MD simulations were consistent with the experimental results, where the hydrophobic unit of IMA was located near the surface of the bilayer membranes and anions remained near the C2 proton of the imidazolium ring during anion transportation. In addition, IMA is suggested to form dimeric complexes with anions within the lipid bilayer membranes. Upon changing the anions and cations of the buffer solution in ion transport assays, IMA most efficiently transported NO₃⁻, an anion considered to play important roles in several biological events.^[3] We believe that the imidazolium-based multiblock structural motif would contribute to the development of synthetic anion transporters.

Experimental Section

Materials

DOPC, DPPC, 5-doxy PC, 12-doxy PC and 16-doxy PC were purchased from Avanti Polar Lipids. TMSA, triisopropylsilane, glyoxal, Pd(PPh₃)₂Cl₂, CH(OEt)₃, 4-iodo-phenol, 2,6-dimethylaniline, BTMA-ICl₂, NaBH₄, HPTS, FCCP and TBANO₃ were purchased from Tokyo Chemical Industry. TBACl, CuI, TsOH·H₂O, K₂CO₃, CaCO₃, NaHSO₃, anhydrous Na₂SO₄, HEPES and salts used for buffers were purchased from Nacalai Tesque. HCOOH, NH₄BF₄ and NaClO₄ were purchased from Wako Pure Chemical Industries. Lucigenin and Et₃N were purchased from Sigma-Aldrich. Valinomycin was purchased from abcam. Anhydrous DMF and THF were purchased from Kanto Chemical and passed through two sequential drying columns on a Glass-Contour system immediately prior to use. Deionized water (filtered through a 0.22 μm membrane filter, > 18.2 MΩcm) was purified in a Milli-Q system of Millipore. Silica gel column chromatography was carried out with Silica Gel 60 (spherical, neutral, particle size: 63–210 μm) purchased from Kanto Chemical. Analytical TLC was performed on precoated, glass-backed silica gel, Merck 60 F254. Visualization of the developed chromatogram was performed by UV absorbance or iodine. Gel permeation chromatography (GPC) was performed on JAI LaboACE LC-5060. CHCl₃ used for GPC was purchased from Nacalai Tesque. Spectra/Por Dialysis Membrane (MWCO 3500) was purchased from Funakoshi.

Measurements

¹H and ¹³C NMR spectra were recorded on Bruker biospin AVANCE III 400 or Bruker biospin AVANCE III HD500. The chemical shifts were determined with respect to tetramethylsilane (TMS), or a residual non-deuterated solvent as an internal standard. Matrix-assisted laser desorption/ionization time-of-flight mass (MALDI-TOF MS) spectrometry was performed on Bruker UltrafleXtreme in reflector mode, using either α-cyano-4-hydroxycinnamic acid (CHCA) or dithnaol as matrices, and electrospray ionization time-of-flight (ESI-TOF) MS was performed on Bruker Daltonics micrOTOF II. Fluorescence spectra and time course change of fluorescence were recorded on JASCO FP-6500 spectrometer using quartz cell of 10 mm optical path length. Large unilamellar vesicles were prepared using Avanti Mini Extruder with 100 nm polycarbonate membranes.

Synthesis

Synthesis of 3: To a dry acetone (55 mL) solution of Trt-PEG₈-Ts^[16] (5.06 g, 6.59 mmol) was added 2 (1.88 g, 9.87 mmol) and K₂CO₃ (2.95 g, 21.3 mmol) at room temperature under Ar, and the resulting mixture was refluxed for 9 h. Then, the reaction mixture was filtered, and the resulting solution was evaporated to dryness under reduced pressure. Brine was added to the residue, and the resulting mixture was then extracted with CHCl₃ for four times. The organic extract was dried over anhydrous Na₂SO₄ and evaporated to dryness under reduced pressure. The crude product was purified by silica gel column chromatography with hexane and EtOAc (3/7 to 0/10) to afford a mixture of 3 and its TMS protected derivative (4.00 g). To a dry MeOH (40 mL) solution of this mixture (4.00 g) was added K₂CO₃ (2.05 g, 14.83 mmol), at room temperature under Ar, and the resulting mixture was stirred for 5 h. The solution was evaporated to dryness under reduced pressure. Sat. NaHCO₃ aq. was added to the residue, and the resulting mixture was then extracted with CHCl₃ for three times. The organic extract was dried over anhydrous Na₂SO₄ and evaporated to dryness under reduced pressure. The crude product was purified by silica gel column

chromatography with hexane and EtOAc (2/8 to 0/10) to allow isolation of **3** (3.71 g, 5.20 mmol) as yellow oil in 78% yield (for two steps). ¹H NMR (400 MHz, CDCl₃ containing 0.03% TMS, 23 °C): δ 7.46 (d, *J* = 7.3 Hz, 6H), 7.41 (d, *J* = 8.8 Hz, 2H), 7.29 (t, *J* = 7.6 Hz, 6H), 7.22 (t, *J* = 7.1 Hz, 3H), 6.85 (d, *J* = 8.8 Hz, 2H), 4.12 (t, *J* = 4.8 Hz, 2H), 3.84 (t, *J* = 4.9 Hz, 2H), 3.72–3.62 (m, 26H), 3.23 (t, *J* = 5.2 Hz, 2H), 2.98 (s, 1H) ppm; ¹³C NMR (125 MHz, CDCl₃ containing 0.03% TMS, 25 °C): δ 159.3, 144.3, 133.7, 128.9, 127.9, 127.1, 114.7, 114.5, 86.7, 83.8, 76.0, 71.0, 70.9, 70.8, 70.7, 69.8, 67.6, 63.5 ppm; ESI-TOF MS (MeOH, positive mode): *m/z*: calculated for C₄₃H₅₂O₉: 712.36; found: 735.60 [M + Na]⁺, 751.57 [M + K]⁺.

Synthesis of 4: To a MeOH/THF = 14/1 (1.5 mL) solution of **3** (527 mg, 0.739 mmol) was added triisopropylsilane (117 mg, 0.741 mmol) and TsOH·H₂O (6 mg, 0.031 mmol) at room temperature, and the reaction mixture was stirred in dark for 9 h. Sat. NaHCO₃ aq. was added to the mixture, and the resulting mixture was stirred for 5 min and evaporated under reduced pressure to remove organic solvents. Then, the resulting mixture was extracted with CHCl₃ for three times. The organic extract was washed with brine, dried over anhydrous Na₂SO₄ and evaporated to dryness under reduced pressure. The crude product was purified by silica gel column chromatography with EtOAc and MeOH (100/0 to 90/10) to allow isolation of **4** (208 mg, 0.442 mmol) as colorless oil in 59% yield. ¹H NMR (400 MHz, CDCl₃ containing 0.03% TMS, 24 °C): δ 7.41 (d, *J* = 8.9 Hz, 2H), 6.85 (d, *J* = 8.9 Hz, 2H), 4.13 (t, *J* = 4.8 Hz, 2H), 3.85 (t, *J* = 4.9 Hz, 2H), 3.73–3.59 (m, 28H), 2.99 (s, 1H) ppm; ¹³C NMR (125 MHz, CDCl₃ containing 0.03% TMS, 25 °C): δ 159.3, 133.7, 114.7, 114.5, 83.8, 76.0, 72.7, 71.0, 70.8, 70.7, 70.5, 69.8, 67.6, 61.9 ppm; ESI-TOF MS (MeOH, positive mode): *m/z*: calculated for C₂₄H₃₈O₉: 470.25; found: 493.25 [M + Na]⁺.

Synthesis of 6: To a solution of 2,6-dimethylaniline (2.95 g, 24.3 mmol) in CH₂Cl₂/MeOH = 5/2 (415 mL) were added BTMA·Cl₂ (9.35 g, 26.8 mmol) and CaCO₃ (3.96 g, 39.6 mmol) at room temperature, and the resulting mixture was stirred for 1.5 h. The excess CaCO₃ was filtered off, and the filtrate was evaporated to remove organic solvents. 10% NaHSO₃ aq was added to the residue, and the resulting mixture was extracted with *t*-butylmethyl ether for four times. The organic extract was dried over anhydrous Na₂SO₄, evaporated and vacuumed to afford crude brown solids, which were purified by repeated recrystallization in hexane to afford **6** as pale yellow needle-like crystals in 92% yield (5.55 g, 22.4 mmol). ¹H NMR (400 MHz, CDCl₃ containing 0.03% TMS, 25 °C): δ 7.27 (s, 2H), 3.58 (br 2H), 2.13 (s, 6H) ppm; ¹³C NMR (125 MHz, CDCl₃ containing 0.03% TMS, 25 °C): δ 142.7, 136.6, 124.3, 79.3, 17.4 ppm; ESI-TOF MS (MeOH, positive mode): *m/z*: calculated for C₈H₁₀N: 246.98; found: 247.99 [M + H]⁺.

Synthesis of 7: To a solution of **6** (1.99 g, 8.05 mmol) in EtOH (16 mL) were added 39% aqueous solution of glyoxal (602 μL, 4.04 mmol) and catalytic amount of HCOOH (ca. 42 μL) at room temperature. After the reaction mixture was stirred for 17 h, the resulting yellow precipitate was collected by filtration and washed with cold MeOH to allow isolation of **7** as yellow solids in 60% yield (1.27 g, 2.46 mmol). ¹H NMR (400 MHz, CDCl₃ containing 0.03% TMS, 24 °C): δ 8.05 (s, 2H), 7.43 (s, 4H), 2.12 (s, 12H) ppm; ¹³C NMR (125 MHz, CDCl₃ containing 0.03% TMS, 25 °C): δ 163.7, 149.6, 137.1, 129.0, 89.2, 18.0 ppm; ESI-TOF MS (MeOH, positive mode): *m/z*: calculated for C₁₈H₁₈N₂: 515.95; found 538.94 [M + Na]⁺.

Synthesis of 8. To a solution of **7** (1.27 g, 2.46 mmol) in THF/MeOH = 5/1 (14 mL) was added NaBH₄ (210 mg, 5.55 mmol) at 0 °C in ice bath. Then the reaction mixture was stirred for 4 h at room temperature, and the resulting mixture was evaporated to remove organic solvents. Sat. NH₄Cl aq. was added to the residue, and the resulting mixture was then extracted with Et₂O for three times. The organic extract was dried over anhydrous Na₂SO₄ and evaporated

to dryness under reduced pressure. The crude product was purified by silica gel column chromatography with hexane and EtOAc (6/1) as an eluent, followed by recrystallization in hexane to yield 67% of **8** as colorless plate-like crystals (859 mg, 1.65 mmol). ¹H NMR (400 MHz, CDCl₃ containing 0.03% TMS, 24 °C): δ 7.31 (s, 4H), 3.29 (br, 2H), 3.15 (s, 4H), 2.23 (s, 12H) ppm; ¹³C NMR (125 MHz, CDCl₃ containing 0.03% TMS, 25 °C): δ 149.9, 137.6, 132.0, 85.3, 48.8, 18.4 ppm; ESI-TOF MS (MeOH, positive mode): *m/z*: calculated for C₁₈H₂₂N₂: 519.98; found: 521.07 [M + H]⁺, 543.06 [M + Na]⁺.

Synthesis of 9: A mixture of **8** (537 mg, 1.03 mmol), NH₄BF₄ (107 mg, 1.02 mmol) and triethyl orthoformate (13 mL) was stirred at 120 °C for overnight. After the mixture was cooled down to room temperature, Et₂O was added to the mixture. The resulting precipitate was filtered off, and purified by repeated recrystallization in MeOH to allow isolation of **9** as pale orange solids in 50% yield (321 mg, 0.52 mmol). ¹H NMR (400 MHz, DMSO, 23 °C): δ 8.97 (s, 1H), 7.70 (s, 4H), 4.44 (s, 4H), 2.34 (s, 12H) ppm; ¹³C NMR (125 MHz, DMSO, 25 °C): δ 160.2, 138.2, 137.3, 133.2, 96.8, 50.7, 16.7 ppm; ESI-TOF MS (MeOH, positive mode): *m/z*: calculated for C₁₉H₂₁N₂⁺: 530.97; found: 530.96 [M]⁺.

Synthesis of IMA: **4** was freeze dried, and Et₃N was degassed prior to use. To a solution of **4** (89 mg, 0.19 mmol) in Et₃N (0.6 mL) and dry DMF (0.25 mL) were added Pd(PPh₃)₂Cl₂ (17 mg, 0.025 mmol), CuI (4 mg, 0.021 mmol), **9** (47 mg, 0.076 mmol) and dry DMF (0.2 mL), and the resulting mixture was stirred for 1.5 h at room temperature in dark. The resulting mixture was dried under reduced pressure, and the residue was purified by silica gel column chromatography with CH₂Cl₂ and MeOH (95/5 to 93/7), followed by gel permeation chromatography with CHCl₃ to allow isolation of **IMA** as yellow oil in 44% yield (43 mg, 0.033 mmol). ¹H NMR (500 MHz, CDCl₃ containing 0.03% TMS, 25 °C): δ 8.33 (s, 1H), 7.45 (d, *J* = 8.5 Hz, 4H), 7.36 (s, 4H), 6.91 (d, *J* = 8.5 Hz, 4H), 4.69 (s, 4H), 4.16 (t, *J* = 4.7 Hz, 4H), 3.87 (t, *J* = 4.7 Hz, 4H), 3.65–3.74 (m, 52H), 3.60 (t, *J* = 4.6 Hz, 4H), 2.62 (t, *J* = 6.3 Hz, 2H), 2.47 (s, 12H) ppm; ¹³C NMR (125 MHz, CDCl₃ containing 0.03% TMS, 25 °C): δ 159.25, 159.02, 135.61, 133.23, 132.17, 131.69, 126.27, 114.77, 114.69, 91.76, 86.74, 72.50, 70.84, 70.60, 70.54, 70.29, 69.61, 67.51, 61.68, 52.14, 18.24 ppm; HRMS (ESI⁺): *m/z*: calculated for C₆₇H₉₅N₂O₁₈⁺: 1215.6574; found: 1215.6546 [M]⁺. See also Figures S19–S21 for NMR and MS spectra.

Preparation of DOPC LUVs for HPTS assay. A CHCl₃ solution of DOPC (10 mM) was evaporated in a glass tube to form a thin lipid film. The film was dried for at least 1 h under vacuum and hydrated with a HEPES buffer (20 mM HEPES, 50 mM NaCl, 30 μM HPTS, pH 7.1, the same volume as CHCl₃, the final concentration of DOPC: 10 mM) at 37 °C. The resulting mixture was vortexed, followed by freezing and thawing (5 cycles), incubated at 37 °C for at least 1 h, and then extruded through a 100-nm membrane for 21 times at room temperature. The obtained suspension was dialyzed by a HEPES buffer (20 mM HEPES, 50 mM NaCl, pH 7.1) at room temperature using Spectra/Por Dialysis Membrane (MWCO 3500).

Concentration dependency on ion transport. To a HEPES buffer (1.96 mL, 20 mM HEPES, 50 mM NaCl, pH 7.9) in a clean quartz cell of 10 mm optical path length was added DOPC LUVs suspension containing HPTS (40 μL) prepared above. The cell was set to the fluorescence spectrometer equipped with a magnetic stirrer at 20 °C (*t* = 0). Time course change of the fluorescence intensity was measured at λ_{em} = 510 nm (λ_{ex} = 460 nm). An aqueous solution of **IMA** (0–1.5 mM, 10 μL) was added at *t* = 10 s, followed by addition of 10%wt TritonX-100 (15 μL) at *t* = 210 s to cause lysis for complete disruption of the pH gradient. Normalized fluorescence intensities in Figures 1–3 were calculated following the equation 1, where *I_t*, *I₀*, and *I_{lysed}* represent fluorescence intensity at *t* (s) after the addition

of IMA, before the addition of IMA ($t=0$) and after the lysis by the addition of 10%wt Triton X-100, respectively.

$$I = I_t - I_0 / I_{lysed} - I_0 \quad (1)$$

Hill analysis. Hill coefficient (n) and effective concentration (EC_{50}) were calculated using the equation 2,^[17] where Y and $[c]$ represent fluorescence intensity as transmembrane ion transport activity and concentration of IMA, respectively.

$$Y = Y_{\infty} + (Y_0 - Y_{\infty}) / (1 + (c/EC_{50})^n) \quad (2)$$

Ion selectivity assay. To a HEPES buffer (1.96 mL, 20 mM HEPES, pH 7.9) including 50 mM MCl ($M=Li^+, Na^+, K^+, Rb^+, Cs^+$ for cation selectivity assay) or 50 mM NaX ($X=Cl^-, Br^-, I^-, NO_3^-, ClO_4^-$ for anion selectivity assay) in a clean quartz cell of 10 mm optical path length, was added a DOPC LUVs suspension containing HPTS (40 μ L) prepared above. The cell was set to the fluorescence spectrometer equipped with magnetic stirrer at 20 °C ($t=0$). Time course change of fluorescence intensity I_t was measured at $\lambda_{em}=510$ nm ($\lambda_{ex}=460$ nm). An aqueous solution of IMA (400 μ M, 10 μ L) was added to the cuvette at $t=10$ s, and 10%wt TritonX-100 (15 μ L) was added at $t=210$ s to induce lysis for complete disruption of pH gradient.

FCCP assay. To a HEPES buffer (1.96 mL, 20 mM HEPES, 50 mM NaCl, pH 7.9) in a clean quartz cell of 10 mm optical length was added a DOPC LUVs suspension encapsulating HPTS (40 μ L). The cell was set to the fluorescence spectrometer equipped with a magnetic stirrer at 20 °C ($t=0$). Time course change of fluorescence intensity was measured at $\lambda_{em}=510$ nm ($\lambda_{ex}=460$ nm). A DMSO solution of FCCP (400 μ M, 5 μ L) was added at $t=10$ and an aqueous solution of IMA (400 μ M, 10 μ L) was added at $t=50$, followed by addition of 10%wt TritonX-100 (15 μ L) at $t=250$ to induce lysis for complete disruption of pH gradient. The data shown in Figure 3b were normalized following the eq. (1), where I_0 is the fluorescence intensity just before the addition of IMA.

Valinomycin assay. To a HEPES buffer (1.96 mL, 20 mM HEPES, 50 mM KCl, pH 7.9) in a clean quartz cell of 10 mm optical length was added a DOPC LUVs suspension encapsulating HPTS (40 μ L). The cell was set to the fluorescence spectrometer equipped with a magnetic stirrer at 20 °C ($t=0$). Time course change of fluorescence intensity was measured at $\lambda_{em}=510$ nm ($\lambda_{ex}=460$ nm). A DMSO solution of valinomycin (5 nM, 5 μ L) was added at $t=10$ and an aqueous solution of IMA (400 μ M, 10 μ L) was added at $t=50$, followed by addition of 10%wt TritonX-100 (15 μ L) at $t=250$ to induce lysis for complete disruption of pH gradient. The data shown in Figure 3d were normalized following the eq. (1), where I_0 is the fluorescence intensity just before the addition of IMA.

Preparation of DOPC LUVs for lucigenin assay. DOPC LUVs encapsulating lucigenin dye was prepared following the same procedures as the HPTS assay, using a HEPES buffer (20 mM HEPES, 50 mM NaNO₃, 300 μ M lucigenin, pH 7.1). Dialysis was carried out with a HEPES buffer (20 mM HEPES, 50 mM NaNO₃, pH 7.1) at room temperature using Spectra/Por Dialysis Membrane (MW3500).

Lucigenin assay. To a HEPES buffer (1.96 mL, 20 mM HEPES, 50 mM NaNO₃, pH 7.1) in a clean quartz cell of 10 mm optical path length was added a DOPC LUVs suspension encapsulating lucigenin (40 μ L) prepared above. The cell was set to the fluorescence spectrometer equipped with a magnetic stirrer at 20 °C ($t=0$). Time course change of fluorescence intensity was measured at $\lambda_{em}=535$ nm ($\lambda_{ex}=450$ nm). NaCl aq. (2 M, 10 μ L) was added at $t=10$, an aqueous solution of IMA (0–1.5 mM, 10 μ L) was added at $t=50$,

and finally, 10%wt TritonX-100 (15 μ L) was added at $t=250$ to induce lysis for complete disruption of chloride gradient.

Preparation of DPPC LUVs for HPTS assays. A CHCl₃ solution of DPPC (10 mM) was evaporated in a glass tube to form a thin lipid film. The film was dried for at least 1 h under vacuum and hydrated with a HEPES buffer (20 mM HEPES, 50 mM NaCl, 30 μ M HPTS, pH 7.1, the same volume as CHCl₃, the final concentration of DPPC: 10 mM) at 50 °C. The resulting mixture was vortexed, followed by freezing and thawing (5 cycles), incubated at 50 °C for at least 1 h, and then extruded through a 100 nm membrane for 21 times at 60 °C. The obtained suspension was dialyzed by a HEPES buffer (20 mM HEPES, 50 mM NaCl, pH 7.1) at room temperature using Spectra/Por Dialysis Membrane (MWCO 3500).

Investigation of carrier mechanism. To a HEPES buffer (1.96 mL, 20 mM HEPES, 50 mM NaCl, pH 7.1) in a clean quartz cell of 10 mm optical path was added a DPPC LUV suspension encapsulating HPTS (40 μ L) prepared above. The cell was set to the fluorescence spectrometer equipped with a magnetic stirrer, and stirred at 50 °C for 2 min. Then an aqueous solution of IMA (50 μ M, 10 μ L) was added to the resulting solution. For the measurement at the liquid phase (50 °C), the sample solution was stirred at 50 °C for 30 s prior to measurement ($t=0$). As for the measurement at the gel phase (20 °C), the sample solution was stirred at 50 °C for 30 s, and then cooled down to 20 °C for 4 min to equilibrate the sample solution ($t=0$). A NaOH aq. solution (0.6 M, 32 μ L) was added to create pH gradient at $t=30$, followed by addition of 10%wt TritonX-100 (20 μ L) at $t=230$ to induce lysis for complete disruption of pH gradient. The data shown in Figure 3f were normalized following the eq. (1), where I_0 is the fluorescence intensity just before the addition of NaOH aq.

¹H NMR titration. IMA, TBAX ($X=Cl$ or NO_3) was dried under vacuum before preparing the stock solutions. Then stock solutions of 2 mM IMA, and 40 mM, 20 mM, 10 mM or 5 mM TBAX in CDCl₃ were prepared individually. An IMA solution (250 μ L) and the TBAX solutions were mixed in a NMR tube, and CDCl₃ was added to adjust a total volume of the sample solution to 500 μ L where the concentration of IMA was fixed to 1 mM. The NMR tubes were sealed tightly through the measurement. NMR measurements were carried out at 25 °C using Bruker biospin AVANCE III HD500.

Fluorescence depth quenching. A CHCl₃ solution of DOPC (10 mM, 150 μ L) or a CHCl₃ solution of a mixture of DOPC (10 mM, 135 μ L) and 5-, 12-, or 16-doxyl PC (1 mM, 135 μ L) ([DOPC/doxyl PC]=9/1) in a glass tube was evaporated to form a thin lipid film. The resulting films were dried under vacuum for 1 h and hydrated with a HEPES buffer (20 mM HEPES, 50 mM NaCl, pH 7.1, 1.5 mL, the final concentration of phospholipids: 1 mM) at 37 °C. The resulting mixture was vortexed followed by freezing and thawing (5 cycles), incubated at 37 °C for 1 h, and then extruded through 100 nm membrane for 21 times. The phospholipids suspension (400 μ L) was diluted with a HEPES buffer (20 mM HEPES, 50 mM NaCl, pH 7.1, 1.6 mL, the final concentration of phospholipids: 200 μ M), followed by addition of an aqueous solution of IMA (1 mM, 10 μ L), and stirred for 30 s at 20 °C for the fluorescent measurements at $\lambda_{ex}=300$ nm.

Modelling of IMA. A three dimensional structure of an IMA was built by 2D Sketcher and Minimize-Selected-Atoms modules in MAESTRO (Shrödinger release 2019-1). One IMA was embedded in DOPC membrane and water molecules using the Membrane Builder implemented in CHARMM-GUI.^[33–38] The imidazolium ring was placed at the center of the lipid bilayer, and the four different initial structures were prepared depending on the orientation of the hydrophobic moiety of the IMA and the presence or absence of Cl⁻: The orientation was set so that the hydrophobic moiety was

perpendicular or parallel to the membrane (Figure S3a-d), and a Cl⁻ was placed near the C2 proton of the imidazolium ring (Figure S3e,f). The unit cell was set to a rectangular cell, and the IMA was embedded in a 50 Å × 50 Å DOPC bilayer at the x-y plane in the center of the cell, and the number of DOPC molecules at the upper and lower leaflets was ~33 and ~34 for the perpendicular model, or ~34 and ~36 for the parallel model, respectively. Along the z-axis direction, the cell was filled with water molecules (TIP3P water model^[39]), and the water thickness was set to 22.5 Å. In addition to the water molecules, counterions (Cl⁻) and 50 mM NaCl were added.

All-atom molecular dynamics (MD) simulations of the IMA embedded in the membrane-water system were carried out. All the MD simulations were performed using the MD program package GROMACS ver. 2016.3^[40-42]. The force field for the membranes and the solvent molecules was the CHARMM36 force field,^[43-47] and that for the IMA was the CHARMM General Force Field (CGenFF).^[48] The electrostatic interaction was handled by the smooth particle mesh Ewald method,^[49] and the van der Waals interaction was truncated by the switching function with the range of 10–12 Å. The bond lengths involving hydrogen atoms were constrained by the P-LINKS algorithm.^[50] Before the production runs, according to the default setups of the CHARMM-GUI, an energy minimization and equilibration runs were executed sequentially. The setups of the equilibration runs were the same as those of our previous simulations.^[14] The production runs were performed with the isothermal-isobaric ensemble and the 2 fs timestep. The temperature and pressure were set to 300 K and 1 atm. The thermostat and the barostat were the Nosé-Hoover scheme^[51,52] and the semi-isotropic Parrinello-Rahman approach,^[53,54] respectively. After the equilibration runs, three independent production runs were performed for each initial structural model. The length of the production run was 1 μs (3 μs for each model, and 12 μs in total). The snapshot was saved every 1 ns.

In addition to the IMA monomer system, the IMA dimer system was prepared. Using the built structure of the IMA described above, one IMA was embedded in DOPC membrane, one Cl⁻ was placed near the C2 proton of the embedded IMA, and the other IMA was placed so that the imidazolium rings of the two IMAs were placed facing each other. The orientation of the IMA dimer was set to the perpendicular or parallel direction to the membrane (Figures S11a,b). The membrane-water system of the IMA dimer model was prepared using the Membrane Builder implemented in CHARMM-GUI^[33-38] with the same condition of the IMA monomer system. All-atom MD simulations of the IMA dimer system were carried out with the same procedure and settings for the monomer system. Three independent 1-μs production runs were performed for each initial dimer structure (3 μs for each model, and 6 μs in total).

Acknowledgements

The authors thank Materials Analysis Division, Open Facility, Tokyo Institute of Technology, for ESI-TOF MS, MALDI-TOF MS, ¹H and ¹³C NMR spectroscopy, and the Open Research Facilities for Life Science and Technology, Tokyo Institute of Technology, for fluorescence spectroscopy. This work was supported by Grand-in-Aid for Scientific Research on Innovative Areas “Molecular Engine (No.8006)” (18H05419 and 18H05418 to KK, 18H05426 to M.I.), Grant-in-Aid for Scientific Research B (19H02831 to KK), “Program for Promoting Researches on the Supercomputer Fugaku” (MD-driven Precision Medicine) (Project ID: hp200129 to M.I.), Platform

Project for Supporting Drug Discovery and Life Science Research (Basis for Supporting Innovative Drug Discovery and Life Science Research (BINDS)) from AMED under Grant Number JP20an0101009 to M.I., and RIKEN Dynamic Structural Biology Project (M.I.).

Conflict of Interest

The authors declare no conflict of interest.

Keywords: Anion transport · mobile carrier · multiblock amphiphile · imidazolium · hydrogen bond

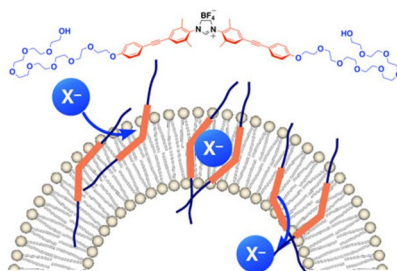
- [1] a) A. Kondratskyi, K. Kondratska, R. Skryma, N. Prevarskaya, *Biochim. Biophys. Acta* **2015**, *1848*, 2532–2546; b) F. Lang, M. Föller, K. S. Lang, P. A. Lang, M. Ritter, E. Gulbins, A. Vereninov, S. M. Huber, *J. Membr. Biol.* **2005**, *205*, 147–157; c) N. Prevarskaya, R. Skryma, G. Bidaux, M. Flourakis, Y. Shuba, *Cell Death Differ.* **2007**, *14*, 1295–1304.
- [2] a) R. Planells-Cases, T. J. Jentsch, *Biochim. Biophys. Acta* **2009**, *1792*, 173–189; b) E. Cordat, J. R. Casey, *Biochem. J.* **2009**, *417*, 423–439; c) J. Y. Choi, D. Muallem, K. Kiselyov, M. G. Lee, P. J. Thomas, S. Muallem, *Nature* **2001**, *410*, 94–97; d) D. N. Sheppard, D. P. Rich, L. S. Ostedgaard, R. J. Gregory, A. E. Smith, M. J. Welsh, *Nature* **1993**, *362*, 160–164.
- [3] J. O. Lundberg, M. T. Gladwin, A. Ahluwalia, N. Benjamin, N. S. Bryan, A. Butler, P. Cabrales, A. Fago, M. Feelisch, P. C. Ford, B. A. Freeman, M. Frenneaux, J. Friedman, M. Kelm, C. G. Kevil, D. B. Kim-Shapiro, A. V. Kozlov, J. R. Lancaster Jr., D. J. Lefler, K. McColl, K. McCurry, R. P. Patel, J. Petersson, T. Rassaf, V. P. Reutov, G. B. Richter-Addo, A. Schechter, S. Shiva, K. Tsuchiya, E. E. van Faassen, A. J. Webb, B. S. Zuckerbraun, J. L. Zweier, E. Weitzberg, *Nat. Chem. Biol.* **2009**, *5*, 865–869.
- [4] a) R. Dutzler, E. B. Campbell, R. MacKinnon, *Science* **2003**, *300*, 108–112; b) R. Dutzler, E. B. Campbell, M. Cadene, B. T. Chait, R. MacKinnon, *Nature* **2002**, *415*, 287–294.
- [5] N. Busschaert, P. A. Gale, *Angew. Chem. Int. Ed.* **2013**, *52*, 1374–1382; *Angew. Chem.* **2013**, *125*, 1414–1422.
- [6] a) A. V. Koulou, T. N. Lambert, R. Shukla, M. Jain, J. M. Boon, B. D. Smith, H. Li, D. N. Sheppard, J.-B. Joos, J. P. Clare, A. P. Davis, *Angew. Chem. Int. Ed.* **2003**, *42*, 4931–4933; *Angew. Chem.* **2003**, *115*, 5081–5083; b) N. Busschaert, I. L. Kirby, S. Young, S. J. Coles, P. N. Horton, M. E. Light, P. A. Gale, *Angew. Chem. Int. Ed.* **2012**, *51*, 4426–4430; *Angew. Chem.* **2012**, *124*, 4502–4506; c) S. Matile, A. V. Jentsch, J. Montenegro, A. Fin, *Chem. Soc. Rev.* **2011**, *40*, 2453–2474; d) P. A. Gale, J. T. Davis, R. Quesada, *Chem. Soc. Rev.* **2017**, *46*, 2497–2519; e) I. Alfonso, R. Quesada, *Chem. Sci.* **2013**, *4*, 3009–3019; f) J. T. Davis, O. Okunola, R. Quesada, *Chem. Soc. Rev.* **2010**, *39*, 3843–3862; g) S. Benz, M. Macchione, Q. Verole, J. Mareda, N. Sakai, S. Matile, *J. Am. Chem. Soc.* **2016**, *138*, 9093–9096.
- [7] J. Cai, J. L. Sessler, *Chem. Soc. Rev.* **2014**, *43*, 6198–6213.
- [8] M. Yano, C. C. Tong, M. E. Light, F. P. Schmidtchen, P. A. Gale, *Org. Biomol. Chem.* **2010**, *8*, 4356–4363.
- [9] M. Lisbjerg, H. Valkenier, B. M. Jessen, H. Al-Kerdi, A. P. Davis, M. Pittelkow, *J. Am. Chem. Soc.* **2015**, *137*, 4948–4951.
- [10] J. Shang, W. Si, W. Zhao, Y. Che, J.-L. Hou, H. Jiang, *Org. Lett.* **2014**, *16*, 4008–4011.
- [11] T. Muraoka, T. Shima, T. Hamada, M. Morita, M. Takagi, K. V. Tabata, H. Noji, K. Kinbara, *J. Am. Chem. Soc.* **2012**, *134*, 19788–19794.
- [12] T. Muraoka, K. Umetsu, K. V. Tabata, T. Hamada, H. Noji, T. Yamashita, K. Kinbara, *J. Am. Chem. Soc.* **2017**, *139*, 18016–18023.
- [13] T. Muraoka, T. Endo, K. V. Tabata, H. Noji, S. Nagatoishi, K. Tsumoto, R. Lui, K. Kinbara, *J. Am. Chem. Soc.* **2014**, *136*, 15584–15595.
- [14] T. Muraoka, D. Noguchi, R. S. Kasai, K. Sato, R. Sasaki, K. V. Tabata, T. Ekimota, M. Ikeguchi, K. Kamagata, N. Hoshino, H. Noji, T. Akutagawa, K. Ichimura, K. Kinbara, *Nat. Commun.* **2020**, *11*, 2924.
- [15] K. Sonogashira, Y. Tohda, N. Hagihara, *Tetrahedron Lett.* **1975**, *50*, 4467–4470.
- [16] A. M. Wawro, T. Muraoka, M. Kato, K. Kinbara, *Org. Chem. Front.* **2016**, *3*, 1524–1534.
- [17] S. Bhosale, S. Matile, *Chirality* **2006**, *18*, 849–856.

- [18] For reference, we performed HPTS assay for Chloride ionophore I-Cocktail A under the same conditions. The effective concentration was $EC_{50} = 1.23 (\pm 0.22)$ nM.
- [19] N. Sakai, S. Matile, *J. Phys. Org. Chem.* **2006**, *19*, 452–460.
- [20] B. A. McNally, A. V. Koulou, B. D. Smith, J.-B. Joos, A. P. Davis, *Chem. Commun.* **2005**, 1087–1089.
- [21] T. L. Ho, Hard, *Soft Acids, Bases Principle in Organic Chemistry*, Academic Press, New York, **1977**, pp. 4–7.
- [22] C. Ren, X. Ding, A. Roy, J. Shen, S. Zhou, F. Chen, S. F. Y. Li, H. Ren, Y. Y. Yang, H. Zeng, *Chem. Sci.* **2018**, *9*, 4044–4051.
- [23] S. V. Shinde, P. Talukdar, *Angew. Chem. Int. Ed.* **2017**, *56*, 4238–4242; *Angew. Chem.* **2017**, *129*, 4302–4306.
- [24] C. Ren, X. Ding, A. Roy, J. Shen, S. Zhou, F. Chen, S. F. Y. Li, H. Ren, Y. Y. Yang, H. Zeng, *Chem. Sci.* **2018**, *9*, 4044–4051.
- [25] H. Behera, N. Madhavan, *J. Am. Chem. Soc.* **2017**, *139*, 12919–12922.
- [26] C. R. Elie, G. David, A. R. Schmitzer, *J. Med. Chem.* **2015**, *58*, 2358–2366.
- [27] G. Deng, T. Dewa, S. L. Regen, *J. Am. Chem. Soc.* **1996**, *118*, 8975–8976.
- [28] P. Thordarson, *Chem. Soc. Rev.* **2011**, *40*, 1305–1323.
- [29] D. B. Hibbert, P. Thordarson, *Chem. Commun.* **2016**, *52*, 12792–12805.
- [30] The change in chemical shift of H_b upon addition of NO_3^- to IMA (Figure S2) was also analyzed by BindFit v0.5,^[28,29] where the association constants for 2:1 complexation were evaluated as $K_{11} = 5.80 \times 10^2 M^{-1}$ (error: $\pm 3.03\%$) and $K_{21} = 4.59 \times 10^2 M^{-1}$ (error: $\pm 1.49\%$).
- [31] The curve fitting analysis with chemical shift data of protons other than H_b resulted in poor curve fitting qualities for both Cl^- and NO_3^- .
- [32] L. A. Weiss, N. Sakai, B. Ghebremariam, C. Ni, S. Matile, *J. Am. Chem. Soc.* **1997**, *119*, 12142–12149.
- [33] S. Jo, T. Kim, V. G. Lyer, W. Im, *J. Comput. Chem.* **2008**, *29*, 1859–1865.
- [34] S. Jo, T. Kim, W. Im, *PLoS One* **2007**, *2*, e880.
- [35] S. Jo, J. B. Lim, J. B. Klauda, W. Im, *Biophys. J.* **2009**, *97*, 50–58.
- [36] E. L. Wu, X. Cheng, S. Jo, H. Rui, K. C. Song, E. M. Dávila-Contreras, Y. Qi, J. Lee, V. Monje-Galvan, R. M. Venable, J. B. Kauda, W. Im, *J. Comput. Chem.* **2014**, *35*, 1997–2004.
- [37] J. Lee, X. Cheng, J. M. Swails, M. S. Yeom, P. K. Eastman, J. A. Lemkul, S. Wei, J. Buckner, J. C. Jeong, Y. Qi, S. Jo, V. S. Pande, D. A. Case, C. L. Brooks III, A. D. MacKerell Jr, J. B. Kauda, W. Im, *J. Chem. Theory Comput.* **2016**, *12*, 405–413.
- [38] J. Lee, D. S. Paterl, J. Stähle, S.-J. Park, N. R. Kern, S. Kim, J. Lee, X. Cheng, M. A. Valvano, O. Holst, Y. Knirel, Y. Qui, S. Jo, J. B. Kauda, G. Widmalm, W. Im, *J. Chem. Theory Comput.* **2019**, *15*, 775–786.
- [39] W. L. Jorgensen, J. Chandrasekhar, J. D. Madura, R. M. Impey, M. L. Klein, *J. Chem. Phys.* **1983**, *79*, 926–935.
- [40] M. J. Abraham, T. Murtola, R. Schulz, S. Páll, J. C. Smith, B. Hess, E. Lindahl, *Software X* **2015**, *1*, 19–25.
- [41] S. Páll, M. J. Abraham, C. Kutzner, B. Hess, E. Lindahl, in S. Markidis, E. Laure (Eds.), *Solving software challenges for exascale* **2015**, 3–27.
- [42] S. Pronk, S. Páll, R. Schulz, P. Larsson, P. Bjelkmar, R. Apostolov, M. R. Shirts, J. C. Smith, P. M. Kasson, D. van der Spoel, B. Hess, E. Lindahl, *Bioinformatics* **2013**, *29*, 845–854.
- [43] J. Huang, S. Rauscher, G. Nawrocki, T. Ran, M. Feig, B. L. de Groot, H. Grubmüller, A. D. MacKerell Jr, *Nat. Methods* **2017**, *14*, 71–73.
- [44] A. D. MacKerell, D. Bashford, M. Bellott, R. L. Dunbrack, J. D. Evanseck, M. J. Field, S. Fischer, J. Gao, H. Guo, S. Ha, D. Joseph-McCarthy, L. Kuchnir, K. Kuczera, F. T. Lau, C. Mattos, S. Michnick, T. Ngo, D. T. Nguyen, B. Prodhom, W. E. Reiher, B. Roux, M. Schlenkrich, J. C. Smith, R. Stote, J. Straub, M. Watanabe, J. Wiórkiewicz-Kuczera, D. Yin, M. Karplus, *J. Phys. Chem. B* **1998**, *102*, 3586–3616.
- [45] A. D. MacKerell Jr, M. Feig, C. L. Brooks, *J. Am. Chem. Soc.* **2004**, *126*, 698–699.
- [46] J. B. Klauda, R. M. Venable, J. A. Freites, J. W. O'Connor, D. J. Tobias, C. Mondragon-Ramirez, I. Vorobyov, A. D. MacKerell Jr, R. W. Pastor, *J. Phys. Chem. B* **2010**, *114*, 7830–7843.
- [47] R. M. Venable, A. J. Sodt, B. Rogaski, H. Rui, E. Hatcher, A. D. MacKerell Jr, R. W. Pastor, J. B. Kauda, *Biophys. J.* **2014**, *107*, 134–145.
- [48] W. Yu, X. He, K. Vanommeslaeghe, A. D. MacKerell Jr, *J. Comput. Chem.* **2012**, *33*, 2451–2468.
- [49] U. Essmann, L. Perera, M. L. Berkowitz, T. Darden, H. Lee, L. G. Pedersen, *J. Chem. Phys.* **1995**, *103*, 8577–8593.
- [50] B. Hess, *J. Chem. Theory Comput.* **2008**, *4*, 116–122.
- [51] S. Nosé, *Mol. Phys.* **1984**, *52*, 255–268.
- [52] W. G. Hoover, *Phys. Rev. A* **1985**, *31*, 1695–1697.
- [53] M. Parrinello, A. Rahman, *J. Appl. Phys.* **1981**, *52*, 7182–7190.
- [54] S. Nosé, M. L. Klein, *Mol. Phys.* **1983**, *50*, 1055–1076.

Manuscript received: September 16, 2020
 Revised manuscript received: November 21, 2020
 Accepted manuscript online: November 28, 2020
 Version of record online: ■■■, ■■■■

FULL PAPER

An imidazolinium-based multiblock amphiphile, a mobile carrier capable of transmembrane anion transport with selectivity for nitrate, was developed. It recognizes anions via $(C-H)^+ \cdots X^-$ hydrogen bond of proton at C2 position of the imidazolinium ring.



M. Mori, Dr. K. Sato, Dr. T. Ekimoto*,
S. Okumura, Prof. M. Ikeguchi*,
Prof. K. V. Tabata*, Prof. H. Noji*,
Prof. K. Kinbara**

1 – 12

**Imidazolinium-based Multiblock
Amphiphile as Transmembrane
Anion Transporter**

